



OPEN

Influence of carbon nanotube suspensions on Casson fluid flow over a permeable shrinking membrane: an analytical approach

Rudraiah Mahesh¹, Ulavathi Shettar Mahabaleshwar¹ & Filippos Sofos²✉

The present work employs the single-wall carbon nanotube (SWCNT) and multiwall carbon nanotube (MWCNT) models on axisymmetric Casson fluid flow over a permeable shrinking sheet in the presence of an inclined magnetic field and thermal radiation. By exploiting the similarity variable, the leading nonlinear partial differential equations (PDEs) are converted into dimensionless ordinary differential equations (ODEs). The derived equations are solved analytically, and a dual solution is obtained as a result of the shrinking sheet. The dual solutions for the associated model are found to be numerically stable once the stability analysis is conducted, and the upper branch solution is more stable compared to lower branch solutions. The impact of various physical parameters on velocity and temperature distribution is graphically depicted and discussed in detail. The single wall carbon nanotubes have been found to achieve higher temperatures compared to multiwall carbon nanotubes. According to our findings, adding carbon nanotubes volume fractions to convectional fluids can significantly improve thermal conductivity, and this can find applicability in real world applications such as lubricant technology, allowing for efficient heat dissipation in high-temperatures, enhancing the load-carrying capacity and wear resistance of the machinery.

List of symbols

Latin symbols

A_1, A_2, A_3, A_4, A_5	Constants
B_0	Magnetic field strength [Tesla]
C_p	Specific heat at constant pressure
H_0	Applied magnetic field [wm^{-2}]
k^*	Mean absorption coefficient
M	Magnetic field
N_r	Radiation parameter
Pr	Prandtl number
q_r	Radiative heat flux
q_w	Local heat flux at the wall
T_1	Temperature
V_c	Mass transformation
(r_1, ξ)	Cylindrical coordinate axes
(r_1, ξ, z_1)	Cartesian cylindrical coordinate axes

Greek symbols

Λ	Casson parameter
κ	Thermal conductivity of fluid [$\text{WKg}^{-1}\text{K}^{-1}$]
ξ	Similarity variable
μ_f	Dynamic viscosity [Nsm^{-1}]

¹Department of Studies in Mathematics, Davangere University, Shivangangothri, Davangere 577 007, India. ²Condensed Matter Physics Laboratory, Department of Physics, University of Thessaly, 35100 Lamia, Greece. ✉email: fsofos@uth.gr

ν	Kinematic viscosity [m^2s^{-1}]
ρ	Density [Kgm^{-3}]
σ	Electrical conductivity [s/m]
σ^*	Stefan–Boltzmann constant [$\text{Wm}^{-2}\text{K}^{-2}$]
Γ	Gamma function
φ	Nanoparticle volume fraction
ψ	Stream function
τ	Angle of inclination of magnetic field

Subscripts

f	Base fluid
nf	Nanofluid

Abbreviations

MHD	Magnetohydrodynamics
CNT	Carbon nanotube
SWCNT	Single wall carbon nanotube
MWCNT	Multi-walled carbon nanotube
LT	Laplace transformation

The thermal conductivity of nanofluids has been a popular point of research during the last few decades. The majority of these studies focuses on understanding their properties with the goal of enhancing heat transfer in a variety of commercial and technological applications, including nuclear reactors, power production, material processing, bioengineering, transportation, paper cooling and drying, electronics, medical, and food industry¹. Means of increasing thermal conductivity include the addition of high thermal conductivity materials, usually carbon-based, metal-based, or other structures like silica or boron nitride².

Towards the incorporation of the material that would exhibit excellent thermal properties and mechanical strength³, Sumio Iijima⁴ made a pioneering discovery of cylindrical carbon atom structures with sizes ranging from 1 to 100 nanometers, the Carbon Nanotube (CNT). CNTs achieve increased thermal conductivity, strength, stiffness, and present low density and large surface area-to-volume ratio. They can be classified as single-wall (SWCNTs) or multi-wall (MWCNTs), depending on the number of layers they are consisted of. In comparison to other nanofluids, CNT suspensions achieve better thermal characteristics.

Recently, the effect of CNTs on the magnetohydrodynamics (MHD) flow of a Newtonian⁵ and a non-Newtonian⁶ fluid under radiation and mass transpiration over a stretching/shrinking sheet has been under investigation. Hussain et al.⁷ have shown that SWCNTs are capable of achieving higher temperature values compared to MWCNTs, by incorporating the mixed convection and analysing the effect of the radiation, heat generation/absorption and diffusion species with viscous effect. The impact of CNTs on MHD fluid flow with thermal radiation and heat source/sink over a flat plate stretching/shrinking sheet was also examined by Mahabaleshwar et al.⁸. Other current studies are focused on the Darcy–Forchheimer flow^{9,10}, by investigating the effect of different nanoparticles on a Riga surface and vertical Cleveland z-staggered cavity, while, Batool et al.¹¹ have investigated the micropolar effect on a nanofluid flow through lid driven cavity.

Due to its wide applicability, boundary layer flow analysis is particularly beneficial from a physical perspective. It should be noticed that boundary layer flow over surfaces greatly differs from free flow regime over stationary plates, as shown by Sakiadis^{12,13} and Crane¹⁴. However, the flow medium plays a major role in the whole process. Non-Newtonian fluids have gained increased research interest lately, mainly because of their numerous applications in industrial processes. However, their complicated nature, compared to Newtonian fluids, urges the incorporation of strongly coupled and nonlinear equations to approach. Maxwell, Oldroyd-B, and Jeffrey nanofluids¹⁵, and Williamson nanofluid¹⁶ are among those exploited for thermal conductivity and viscosity estimation, while the Rabinowitsch fluid has been exploited in peristaltic biological applications¹⁷. On the other hand, the Casson fluid has been of practical importance and wide application field, capable of acting like an elastic liquid when there is no flow and just a minor shear stress. Casson¹⁸ pioneered the use of this approach to replicate industrial inks in his work, unblocking the passage to numerous engineering applications¹⁹ and theoretical studies²⁰. Vaidya et al.²¹ have also investigated the consequences of heat transfer on a non-Newtonian fluid flow via a porous axisymmetric tube with slip effects. Similar works focus on the derivation of an analytical solution for non-Newtonian fluid flow through a porous shrinking surface in the presence of radiation at wall temperature²², and the analysis of the thermal performance of Fe_3O_4 and Cu nanoparticles with blood as the base fluid on a Casson substantial with MHD and Hall current effects²³.

Magnetic-driven flows are of paramount importance in engineering, biochemistry, medical applications, the petroleum sector, power generators, magnetic drug targeting, and more^{24–27}. Thermal radiation has a substantial influence on boundary layer flow in high-temperature processes. As it affects cooling rates, the role of heat radiation is critical for assuring product quality. MHD boundary layer flows involve the application of a magnetic force to electrically conducting fluids. This field generates currents and a Lorentz force opposing to the fields. Devi and Devi²⁸ have numerically examined the impact of Lorentz force on a hybrid nanofluid ejected from a stretched sheet. To explore the turbulent force convection heat transport properties of hybrid nanofluid, Shafiq et al.²⁹ has depicted the impact of the Marangoni effect on axisymmetric convective flow by adding the

additional parameter of inclined MHD in Casson fluid on infinite disk. Flows over porous shrinking surfaces and the respective solutions have been also obtained^{30,31}.

On the other hand, Turkyilmazoglu³² has given dual solutions for 2D magneto flow in sheets that are constantly contracting or expanding due to a pair stress fluid. Multiple exact solutions of a water-based graphene nanofluid created by porous shrinking or stretching a sheet with a heat sink or source are given by Aly³³, while Khan et al.³⁴ have obtained the closed-form exact analytical solution for the axisymmetric hybrid nanofluid on a permeable non-linear radially shrinking/stretching sheet. Different model geometries include the investigation of Casson fluid flows past a nonlinear permeable stretching cylinder on a porous medium³⁵, a cylinder of non-uniform radius³⁶, two permeable spheres³⁷, and a rotating disk³⁸.

The field of investigation is enriched by axisymmetric flow cases where the subsequent conditions vary^{39–41}. Turkyilmazoglu has derived the exact solution for the fluid flow problem^{42,43}, while Wahid et al.⁴⁴ have approached the analytical solution of hybrid nanofluid flow with partial slip on permeable stretching surface with the effect of radiation. Stability analysis has been extensively utilised to validate the real solution mathematically, first developed by Merkin⁴⁵, and, on this basis, relevant research has covered both steady and unsteady cases^{46–48}.

The current study aims to dive deeper towards understanding of the mechanisms involved in Casson fluid flows. The main focus is centred around the derivation of the exact dual solutions in the presence of SWCNTs and MWCNTs, saturated with H₂O and over a shrinking surface, under the impact of an inclined MHD, radiation and mass transpiration. The exact multiple solutions for velocity and temperature distribution are discussed in detail and are graphically explained. The key concepts of this analytical investigation can be incorporated in various engineering and industrial applications, concerning medical applications, micro-fluidic devices, nano-fluid pumps, and space technology. In the next Sections, we discuss the physical model of the problem and the respective mathematical solutions, present the stability analysis, results and validation tests are discussed next, and, finally, the key concepts are summarized in the “Conclusions” Section.

Methods

Physical model. Physical modelling of the basic equation considers a two-dimensional axisymmetric non-Newtonian fluid containing SWCNTs and MWCNTs with the impact of inclined magnetic field boundary layer flow and thermal radiation on heat transformed boundary by a nonlinear permeable radially shrinking surface subjected to the plane (r_1, ξ) . Figure 1 presents the physical model on SWCNT and MWCNT nano particles and their cartesian cylindrical coordinates (r_1, ξ, z_1) , where flow is induced while $T_\infty < T_w$. Here, r_1 and z_1 are the coordinates corresponding to the vertical and horizontal direction, and T_∞ and T_w the ambient and surface temperature of the sheet, respectively. The sheet surface’s velocity model is assumed to be $u_w(r_1) = br_1^3$, where b : constant. The external magnetic field acts in the direction normal to surface as $B(r_1) = B_0r_1$. Furthermore, the permeable sheet surface on wall mass transfer of velocity is given by $w_w(r_1) = -r_1v_0$, where v_0 is characterized as sheet porosity. Moreover, the conditions $w_w < 0$ and $v_0 > 0$ are applied to represent the injection, while $w_w > 0$ and $v_0 < 0$ represent mass suction.

The Casson fluid¹⁸ rheological condition of state is given by the following stress tensor:

$$\tau_{ij} = \begin{cases} \left(\mu_b + \frac{\tau_y}{\sqrt{2\pi}} \right) 2e_{ij}\pi > \pi_c, \\ \left(\mu_b + \frac{\tau_y}{\sqrt{2\pi}} \right) 2e_{ij}\pi < \pi_c, \end{cases} \quad (1)$$

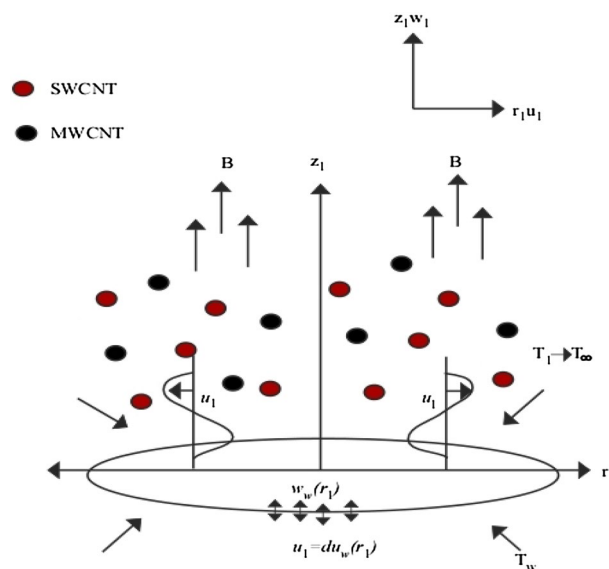


Figure 1. The physical model of the flow.

where τ_y is the yield stress of non-Newtonian Casson fluid, μ_b the plastic dynamic viscosity, $\pi = e_{ij}e_{ij}$, with e_{ij} the $(i, j)^{th}$ element of the deformation rate and π_c the critical value of the deformation rate.

The expression for non-Newtonian Casson fluid τ_y yield stress is

$$\tau_y = \frac{\mu_b \sqrt{2\pi}}{\Lambda} \tag{2}$$

When $\pi > \pi_c$, a Casson fluid flow occurs, and it is possible to state that

$$\mu = \left(\mu_b + \frac{\tau_y}{\sqrt{2\pi}} \right) \tag{3}$$

By substituting Eq. (2) into Eq. (3), we obtain

$$\mu = \mu_b \left(1 + \frac{1}{\Lambda} \right) \tag{4}$$

On the basis of the above information, the convection term in the momentum equation is written as

$$\frac{1}{\rho} \frac{\partial}{\partial y} (\tau_y) = \frac{\mu_b}{\rho} \left(1 + \frac{1}{\Lambda} \right) \frac{\partial^2 u}{\partial y^2} = \nu \left(1 + \frac{1}{\Lambda} \right) \frac{\partial^2 u}{\partial y^2} \tag{5}$$

For CNTs we write the equation as $\nu_{nf} \left(1 + \frac{1}{\Lambda} \right) \frac{\partial^2 u}{\partial y^2}$, where $\nu_{nf} = \frac{\mu_{nf}}{\rho_{nf}}$.

The leading governing equations are (see Ref.³⁴ for details)

$$\frac{\partial u_1}{\partial r_1} + \frac{u_1}{r_1} + \frac{\partial w_1}{\partial z_1} = 0. \tag{6}$$

$$u_1 \frac{\partial u_1}{\partial r_1} + w_1 \frac{\partial u_1}{\partial z_1} = \frac{\mu_{nf}}{\rho_{nf}} \left(1 + \frac{1}{\Lambda} \right) \frac{\partial^2 u_1}{\partial z_1^2} - \frac{\sigma_{nf} B^2(r)}{\rho_{nf}} \sin(\tau) u_1. \tag{7}$$

$$u_1 \frac{\partial T_1}{\partial r_1} + w_1 \frac{\partial T_1}{\partial z_1} = \frac{k_{nf}}{(\rho C_p)_{nf}} \frac{\partial^2 T_1}{\partial z_1^2} - \frac{1}{(\rho C_p)_{nf}} \frac{\partial q_r}{\partial z_1}. \tag{8}$$

where u_1 and w_1 are the velocity components with respect to direction r_1 and z_1 , T_1 the fluid temperature, $\mu_{nf}, \rho_{nf}, \sigma_{nf}, (\rho C_p)_{nf}$ are the dynamic viscosity, density, electrical conductivity, and specific heat of the nano fluid, respectively. The first terms on the right-hand side of Eq. (7) represent the non-Newtonian Casson fluid, and the second term of Eqs. (7) and (8) represents the inclined magnetic field and thermal radiation which can take as radioactive heat flux q_r , respectively.

These equations are subject to the boundary condition:

$$\begin{cases} u_1 = du_w(r_1), & w_1 = w_w(r_1), & T_1 = T_w \text{ at } z_1 = 0, \\ u_1 \rightarrow 0, & T_1 \rightarrow T_\infty, & \text{as } z_1 \rightarrow \infty. \end{cases} \tag{9}$$

where u_1 and w_1 are the velocity components with respect to direction r_1 and z_1 , T_1 the fluid temperature, $u_w(r_1)$ and $w_w(r_1)$ represents the surface's velocity and wall mass transfer of velocity of the sheet, T_∞ and T_w the ambient and surface temperature of the sheet, respectively, d represents the stretching ($d > 0$), shrinking ($d < 0$) and static ($d = 0$) sheet. For the present work we consider only shrinking ($d < 0$) case.

The radioactive heat flux q_r is added to the model by using Rosseland approximations and can be written in the following simplified form, as

$$q_r = \frac{-16\sigma^* T_\infty^3}{3k^*} \frac{\partial T_1^4}{\partial z_1} \tag{10}$$

Then, the term T_1^4 is expanded by using Taylor's series and ignoring higher order terms to obtain

$$T_1^4 = T_{1\infty}^4 + 4T_{1\infty}^3(T_1 - T_{1\infty}) + 6T_{1\infty}^2(T_1 - T_{1\infty})^2 + \dots \tag{11}$$

T_1^4 can be assessed by:

$$T_1^4 \cong -3T_{1\infty}^4 + 4T_{1\infty}^3 T_1. \tag{12}$$

where σ^* is the Stefan-Boltzmann constant and k^* the mean absorption coefficient of base fluid. From Eqs. (8) and (9) we obtain

$$u_1 \frac{\partial T_1}{\partial r_1} + w_1 \frac{\partial T_1}{\partial z_1} = \frac{k_f}{(\rho C_p)_{nf}} \left(\frac{k_{nf}}{k_f} + \frac{16\sigma^* T_\infty^3}{3k^* k_f} \right) \frac{\partial^2 T_1}{\partial z_1^2}. \tag{13}$$

Equivalent density

$$\frac{\rho_{nf}}{\rho_f} = 1 - \phi + \phi \left(\frac{\rho_{CNT}}{\rho_f} \right)$$

Equivalent dynamic

$$\frac{\mu_{nf}}{\mu_f} = \frac{1}{(1-\phi)^{2.5}}$$

Equivalent heat

$$\frac{(\rho cp)_{nf}}{(\rho cp)_f} = 1 - \phi + \phi \left(\frac{(\rho cp)_{CNT}}{(\rho cp)_f} \right)$$

Equivalent electrical

$$\frac{\sigma_{nf}}{\sigma_f} = 1 + \frac{3\phi \left(\frac{\sigma_{CNT}}{\sigma_f} - 1 \right)}{\left(\left(\frac{\sigma_{CNT}}{\sigma_f} + 2 \right) - \left(\frac{\sigma_{CNT}}{\sigma_f} - 1 \right) \phi \right)}$$

Equivalent thermal

$$\frac{k_{nf}}{k_f} = \frac{1 - \phi + 2\phi \left(\frac{k_{CNT}}{k_{CNT} - k_f} \right) \ln \left(\frac{k_{CNT} + k_f}{2k_f} \right)}{1 - \phi + 2\phi \left(\frac{k_f}{k_{CNT} - k_f} \right) \ln \left(\frac{k_{CNT} + k_f}{2k_f} \right)}$$

Figure 2. Thermophysical expressions for CNTs in our model.

Thermophysical expressions and properties of the CNTs. In Fig. 2, ϕ is known as solid volume fraction of nanoparticle, and with the nf as subscript, $\rho_{nf}, \mu_{nf}, \sigma_{nf}, \kappa_{nf}, \rho C p_{nf}$ are the density, viscosity, electrical conductivity, thermal conductivity, heat capacity of the nanofluid, respectively. The f subscript denotes the same quantities, but for the base fluid, while the CNT as subscript refers to the carbon nanofluid. The experimental values of C_p (specific heat), ρ (density), κ (thermal conductivity), and σ (electrical conductivity) for the base fluid (water), SWCNT and MWCNT are presented in Table 1^{6,7}

Similarity variable. We proposed the following similarity variable to simplify the problem,

$$\xi = \sqrt{\frac{b}{\nu_f}} z_1 r_1, \theta(\xi) = \frac{T_1 - T_\infty}{T_w - T_\infty}, \psi = -\sqrt{b \nu_f} r_1^3 f(\xi) \quad (14)$$

where ψ is the stream function, while u_1 and w_1 are given by $u_1 = \frac{1}{r_1} \frac{\partial \psi}{\partial z_1}$ and $w_1 = -\frac{1}{r_1} \frac{\partial \psi}{\partial r_1}$. Taking Eq. (9) into consideration, the velocity components can be written as

$$u_1 = b r_1^3 F'(\xi) \text{ and } w_1 = -\sqrt{b \nu_f} r_1 (3F(\xi) + \xi F'(\xi)) \quad (15)$$

Next, through similarity transformation and thermophysical expressions, Eqs. (7) and (13) are converted into

Physical properties	Fluid phase (water)	SWCNT	MWCNT
C_p (Jkg ⁻¹ K ⁻¹)	4179	425	796
ρ (kgm ⁻³)	997.1	2600	1600
κ (Wm ⁻¹ K ⁻¹)	0.613	6600	3000
σ (Ω/m) ⁻¹	0.05	1×10^7	1×10^7

Table 1. Thermal properties of base fluid and nanoparticles.

$$A_1 \left(1 + \frac{1}{\Lambda} \right) F''' - A_5 M \sin(\tau) F' + A_2 (3FF' - 3F'^2) = 0. \tag{16}$$

$$(A_4 + N_r)\theta'' + 3A_3 \text{Pr} F\theta' = 0. \tag{17}$$

subjected to boundary conditions as follows:

$$\begin{cases} F'(\xi) = d, & F(\xi) = V_c, & \theta(\xi) = 1, & \text{at } \xi = 0, \\ F'(\xi) \rightarrow 0, & \theta(\xi) = 0, & & \text{as } \xi \rightarrow \infty. \end{cases} \tag{18}$$

where,

$$\begin{cases} A_1 = \frac{\mu_{nf}}{\mu_f}, & A_2 = \frac{\rho_{nf}}{\rho_f}, & A_3 = \frac{(\rho C_p)_{nf}}{(\rho C_p)_f}, & A_4 = \frac{k_{nf}}{k_f}, & A_5 = \frac{\sigma_{nf}}{\sigma_f}, \\ M = \frac{\sigma_f B_0^2}{\rho_f b}, & N_r = \frac{16\sigma^* T_\infty^3}{3k_f k^*}, & \text{Pr} = \frac{(\rho C_p)_f \nu_f}{k_f}. \end{cases} \tag{19}$$

Engineering physical quantities of interest. The shear stress coefficient C_f and the local heat transfer number Nu_{z_1} are

$$C_f = \frac{2\mu_{nf} \left(1 + \frac{1}{\Lambda} \right)}{\rho_f u_w^2} \left(\frac{\partial u_1}{\partial z_1} \right)_{z_1=0}, \quad Nu_{z_1} = \frac{r_1 k_{nf}}{k_f (T_w - T_\infty)} \left(\frac{\partial T_1}{\partial z_1} \right)_{z_1=0} \tag{20}$$

By imposing the similarity transformation, we obtain

$$0.5 \text{Re}_{r_1}^{1/2} C_f = \frac{\mu_{nf} \left(1 + \frac{1}{\Lambda} \right)}{\mu_f} F''(0), \quad \text{Re}_{r_1}^{-1/2} Nu_{z_1} = -\frac{k_{nf}}{k_f} \theta'(0) \tag{21}$$

where $\text{Re}_{r_1}^{1/2} = \frac{u_w(r_1)r_1}{\nu_f}$ is the Reynolds number.

Exact solution for momentum equation. The exact analytical solution of Eq. (16) subject to boundary condition from Eq. (18) is

$$F(\xi) = V_c + \frac{d}{\beta} (1 - \text{Exp}[-\beta\xi]). \tag{22}$$

By substituting into Eq. (16) and, also, by considering $\tau = \frac{\pi}{2}$, it is $\sin(\tau) = 1$. We obtain an algebraic quadratic Equation as

$$A_1 \left(1 + \frac{1}{\Lambda} \right) \beta^2 - 3A_2 V_c \beta - (A_5 M + 3A_2 d) = 0. \tag{23}$$

where the roots are

$$\beta = \frac{3V_c A_2 \pm \sqrt{9V_c^2 A_2^2 - 4 \left(1 + \frac{1}{\Lambda} \right) A_1 (-3dA_2 - MA_5)}}{2 \left(1 + \frac{1}{\Lambda} \right) A_1} \tag{24}$$

From Eq. (21), it is clearly shown that the problem has both a lower and an upper branch solution. The velocity component $F'(\xi)$ and the skin friction component $F''(0)$ are given by

$$F'(\xi) = d \text{Exp}[-\beta\xi] \text{ and } F''(0) = -d\beta \tag{25}$$

Exact solution for energy equation. Equation (17) can be modified with aid of Eq. (22), and, by introducing a new parameter $\eta = \frac{\text{Pr}}{\beta^2 [-\beta\xi]}$, it transforms to

$$(A_4 + N_r)\eta \frac{d^2\theta}{d\eta^2} + \left\{ (A_4 + N_r) + A_4 \left(3d\eta - 3 \frac{\text{Pr}}{\beta^2} (d + V_c\beta) \right) \right\} \frac{d\theta}{d\eta} \tag{26}$$

with boundary conditions

$$\theta \left(\frac{\text{Pr}}{\beta^2} \right) = 1, \quad \text{and } \theta(0) = 0. \tag{27}$$

Thus, the outcome of Eq. (26) subject to boundary condition from Eq. (27) in terms of incomplete Gamma function is

$$\theta(\eta) = \frac{\Gamma(j, o) - \Gamma\left(j, \frac{3A_3d}{(A_4+N_r)}\eta\right)}{\Gamma(j, o) - \Gamma\left(j, \frac{3A_3dPr}{(A_4+N_r)\beta^2}\right)} \tag{28}$$

where $j = \frac{3A_3(Prd+V_cPr\beta)}{(A_4+N_r)\beta^2}$.

In terms of the similarity variable ξ , Eq. (28) transforms to

$$\theta(\xi) = \frac{\Gamma(j, o) - \Gamma\left(j, \frac{3A_3d}{(A_4+N_r)}\frac{Pr}{\beta^2}Exp[-\beta\xi]\right)}{\Gamma(j, o) - \Gamma\left(j, \frac{3A_3dPr}{(A_4+N_r)\beta^2}\right)} \tag{29}$$

Then,

$$\theta'(\xi) = \frac{-3^jExp\left[-\left(\frac{3A_3dPr}{(A_4+N_r)\beta^2}Exp[-\beta\xi]\right)\right]\beta\left(\frac{3A_3dPr}{(A_4+N_r)\beta^2}Exp[-\beta\xi]\right)^j}{\Gamma(j, o) - \Gamma\left(j, \frac{3A_3dPr}{(A_4+N_r)\beta^2}\right)} \tag{30}$$

where $j = \frac{3A_3(Prd+V_cPr\beta)}{(A_4+N_r)\beta^2}$.

and

$$-\theta'(0) = \frac{3^jExp\left[-\left(\frac{3A_3dPr}{(A_4+N_r)\beta^2}\right)\right]\beta\left(\frac{3A_3dPr}{(A_4+N_r)\beta^2}\right)^j}{\Gamma(j, o) - \Gamma\left(j, \frac{3A_3dPr}{(A_4+N_r)\beta^2}\right)} \tag{31}$$

Equation (31) is the local heat transfer rate at the wall sheet surface.

Stability analysis. A complete study of the stability of dual solutions for the Eqs. (16-17) along with the boundary conditions in Eq. (18) are performed on a shrinking sheet. Merkin⁴⁵ was the first to propose the stability analysis for the dual solutions and showed that a positive eigenvalue in a dual solution is more stable and dependable than a negative eigenvalue. Next, his work was carried out by Harris et al.⁴⁶, and, recently Hamid et al.⁴⁷, Roşca et al.⁴⁸ who studied the stability of the dual solution on Casson fluid flow on stretching sheet and Khashi'ie et al.⁴⁹ for the axisymmetric flow of a hybrid nanofluid on a radially permeable stretching/shrinking sheet, respectively.

Consider the unsteady Casson fluid flow with the time variable $\varepsilon = r_1^2bt$. Equations (7-8) can be written as

$$\frac{\partial u_1}{\partial t} + u_1 \frac{\partial u_1}{\partial r_1} + w_1 \frac{\partial u_1}{\partial z_1} = \frac{\mu_{nf}}{\rho_{nf}} \left(1 + \frac{1}{\Lambda}\right) \frac{\partial^2 u_1}{\partial z_1^2} - \frac{\sigma_{nf}B^2(r)}{\rho_{nf}} \sin(\tau)u_1 \tag{32}$$

$$\frac{\partial T_1}{\partial t} + u_1 \frac{\partial T_1}{\partial r_1} + w_1 \frac{\partial T_1}{\partial z_1} = \frac{k_{nf}}{(\rho C_p)_{nf}} \frac{\partial^2 T_1}{\partial z_1^2} - \frac{1}{(\rho C_p)_{nf}} \frac{\partial q_r}{\partial z_1} \tag{33}$$

By incorporating Eqs. (7-8) we introduce the new dimensionless variable

$$u_1 = br_1^3F'(\xi, \varepsilon), \quad w_1 = -\sqrt{bv_f r_1}(3F(\xi, \varepsilon) + \xi F'(\xi, \varepsilon)), \tag{34}$$

$$\xi = \sqrt{\frac{b}{v_f}}z_1r_1, \quad \theta(\xi, \varepsilon) = \frac{T_1 - T_\infty}{T_w - T_\infty}, \quad \varepsilon = r_1bt,$$

and by adding the new similarity variable to Eq. (34) and taking $\tau = \frac{\pi}{2}$, then $\sin(\tau) = 1$, the following system of Equations is obtained, as

$$A_1 \left(1 + \frac{1}{\Lambda}\right) \frac{\partial^3 F}{\partial \xi^3} + 3A_2F \frac{\partial^2 F}{\partial \xi^2} - 3A_2 \left(\frac{\partial F}{\partial \xi}\right)^2 - A_5M \frac{\partial F}{\partial \xi} - A_2 \frac{\partial^2 F}{\partial \xi \partial \varepsilon} = 0, \tag{35}$$

$$(A_4 + N_r) \frac{\partial^2 \theta''}{\partial \xi^2} + 3A_3 Pr F \frac{\partial \theta}{\partial \xi} - A_3 Pr \frac{\partial \theta}{\partial \varepsilon} = 0, \tag{36}$$

and the boundary condition becomes

$$\begin{cases} \frac{\partial F}{\partial \xi} = d, & F(\xi, \varepsilon) = V_c, & \theta(\xi, \varepsilon) = 1, & \text{at } \xi = 0, \\ \frac{\partial F}{\partial \xi} \rightarrow 0, & \theta(\xi, \varepsilon) = 0, & & \text{as } \xi \rightarrow \infty. \end{cases} \tag{37}$$

Equation (36) is introduced by using the notion in Refs.^{43,44} to test the stability of the dual solutions by considering $F(\xi) = F_0(\xi)$ and $\theta(\xi) = \theta_0(\xi)$, and in the current analysis we have obtained the unsteady form of the Casson fluid on the shrinking sheet as

$$\begin{cases} F(\xi, \varepsilon) = F_0(\xi) + \text{Exp}[-\gamma\xi]f(\xi, \varepsilon), \\ \theta(\xi, \varepsilon) = \theta_0(\xi) + \text{Exp}[-\gamma\xi]\varphi(\xi, \varepsilon), \end{cases} \quad (38)$$

where γ is known as unidentified eigenvalue and $f(\xi, \varepsilon)$ and $\varphi(\xi, \varepsilon)$ are assumed to be smaller than $F_0(\xi)$ and $\theta_0(\xi)$. The unstable solution of Eqs. (33–35) results in an infinite value of (γ) eigenvalue. Initial instability increase relates to a negative eigenvalue, but initial instability decline relates to a positive eigenvalue which implies that the Casson fluid flow over the surface is stable. The unsteady form of the system of differential equations along with boundary condition follow,

$$A_1 \left(1 + \frac{1}{\Lambda}\right) \frac{\partial^3 f}{\partial \xi^3} + 3A_2 F_0 \frac{\partial^2 f}{\partial \xi^2} + 3A_2 f F_0'' - A_2 (6F_0' - \gamma) \frac{\partial f}{\partial \xi} - A_5 M \frac{\partial f}{\partial \xi} - A_2 \frac{\partial^2 F}{\partial \xi \partial \varepsilon} = 0, \quad (39)$$

$$(A_4 + N_r) \frac{\partial^2 \varphi}{\partial \xi^2} + 3A_3 \text{Pr} F_0 \frac{\partial \varphi}{\partial \xi} + 3A_3 \text{Pr} f \theta_0' + \gamma \varphi - A_3 \text{Pr} \frac{\partial \varphi}{\partial \varepsilon} = 0, \quad (40)$$

$$\begin{cases} \frac{\partial f}{\partial \xi} = 0, & f(\xi, \varepsilon) = 0, & \varphi(\xi, \varepsilon) = 0, & \text{at } \xi = 0, \\ \frac{\partial f}{\partial \xi} \rightarrow 0, & \varphi(\xi, \varepsilon) \rightarrow 0, & \text{as } \xi \rightarrow \infty. \end{cases} \quad (41)$$

The generalized linear eigenvalue problem with the boundary conditions is derived by substituting $\varepsilon = 0$ in Eqs. (37–39), which represents the solution in a stable state.

$$A_1 \left(1 + \frac{1}{\Lambda}\right) f_0''' + 3A_2 F_0 f_0'' + 3A_2 f_0 F_0'' - A_2 (6F_0' - \gamma) f_0' - A_5 M f_0' = 0, \quad (42)$$

$$(A_4 + N_r) \varphi_0'' + 3A_3 \text{Pr} F_0 \varphi_0' + 3A_3 \text{Pr} f_0 \theta_0' + \gamma \varphi_0 = 0, \quad (43)$$

$$\begin{cases} \frac{\partial f_0}{\partial \xi} = 0, & f_0(\xi) = 0, & \varphi_0(\xi) = 0, & \text{at } \xi = 0, \\ \frac{\partial f_0}{\partial \xi} \rightarrow 0, & \varphi_0(\xi) \rightarrow 0, & \text{as } \xi \rightarrow \infty. \end{cases} \quad (44)$$

The stability of the relevant solution F_0 and θ_0 is determined by calculating the least value of the eigenvalue for the specific value of Λ , N_r , M , γ , Pr . In this investigation, we swapped out the equivalent boundary condition at free stream $f_0' \rightarrow 0$ as $\xi \rightarrow \infty$ for $f_0''(0) = 1$.

Ethical approval. This article does not contain any studies with human participants or animals performed by any of the authors.

Results and discussion

In the present paper, we have argued on the closed form of the exact analytical dual branch solution for SWCNTs and MWCNTs. Graphical results for various values of V_c , M , N_r , ϕ and d , are to be shown next. The computations are made for $\phi = 0.1$, $V_c = 2.4$, $d = -1.1$, $M = 0.1$, $N_r = 1$ and $\Lambda = 1$, while the thermophysical properties of water and CNTs are taken from Table 1. Note that the Prandtl number of the base fluid (water) is equal to 6.2.

The solution obtained in this analysis is in the form of upper and lower branch solution which are represented graphically in first and second solution, respectively. From the results obtained we come in conclusion that the upper branch solution is more stable than the lower branch solution.

Velocity and temperature profiles. Figures 3 and 4 show the effect of V_c on the velocity and temperature profiles of SWCNT and MWCNT, respectively. It is observed that the velocity of the upper branch solution, both for SWCNT and MWCNT, increases with as V_c increases, too. Moreover, SWCNT attains higher velocity values compared to MWCNT. In contradistinction, the reverse behaviour is observed for the lower branch solution, where the velocity decreases with as V_c increases. This is due to the fact that by increasing V_c , the fluid near the surface is being pulled up more quickly, producing the faster fluid velocity. Another point worth mentioning is that the temperatures of SWCNTs and MWCNTs, for both upper and lower branch solutions, present similar behaviour, as they decrease with increasing V_c . Also, MWCNTs have overall achieved lower temperature compared to SWCNTs, owing to fluid flow over the permeable plate, which removes the highly heated fluid.

The effect of the application of the inclined magnetic field M on velocity and temperature profiles is depicted in Figs. 5 and 6. Different behaviour is observed between SWCNT and MWCNT. In Fig. 5 (upper branch solution), for higher values of M , the velocity of both SWCNT and MWCNT increases, with SWCNT reaching slightly higher values compared to MWCNT. However, in the lower branch, the velocity of SWCNT and

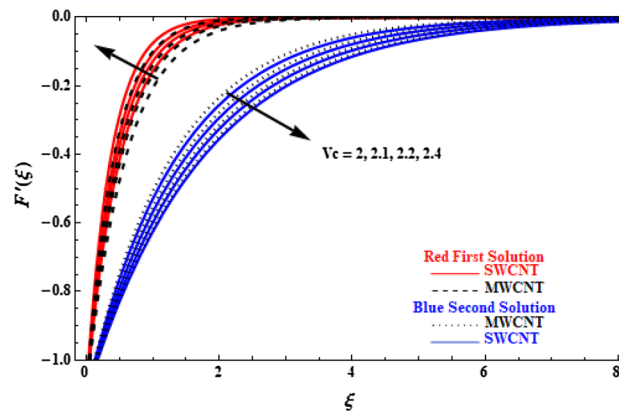


Figure 3. Plot of velocity $F'(\xi)$ versus ξ for various V_c values.

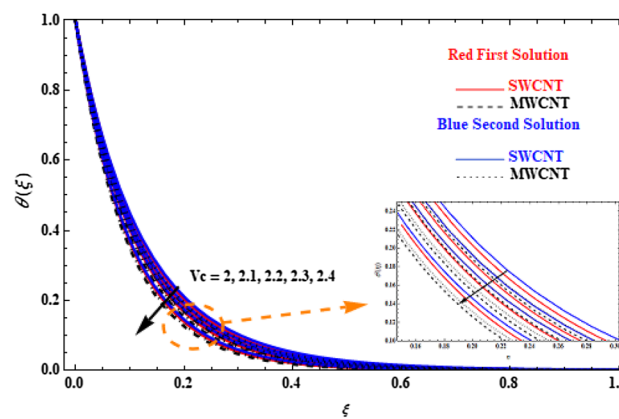


Figure 4. Plot of temperature $\theta(\xi)$ versus ξ for various V_c values.

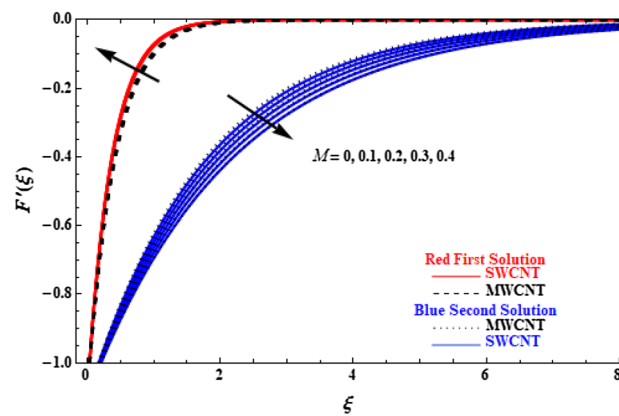


Figure 5. Plot of velocity $F'(\xi)$ versus ξ for various values of M .

MWCNT decreases as M increases, while SWCNT has smaller velocity values compared to MWCNT. In Fig. 6, the temperature of the upper branch solutions is decreased when M increases, but opposite behaviour is observed in the second branch solution, since MWCNT has generally lower temperatures compared to SWCNT. This is attributed to the fact that nanoparticles are greatly influenced by the magnetic field, and higher values of M lead to velocity increase and the fluid temperature decrease.

Velocity and temperature profiles of SWCNT and MWCNT are further examined on the effect of the Casson parameter Λ in Figs. 7 and 8. It is shown that the upper branch solution velocity of SWCNT and MWCNT increases when Λ increases, with MWCNT cases presenting lower velocity values than SWCNT, and, the reverse

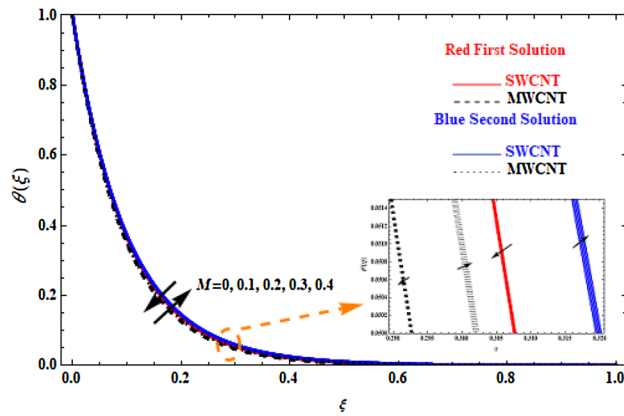


Figure 6. Plot of temperature $\theta(\xi)$ versus ξ for various values of M .

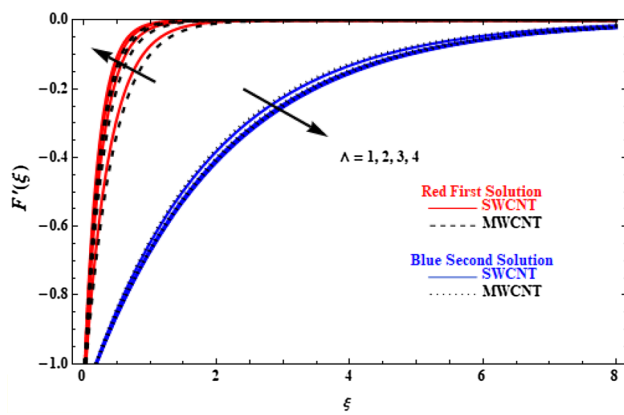


Figure 7. Plot of velocity $F'(\xi)$ versus ξ for various values of Λ .

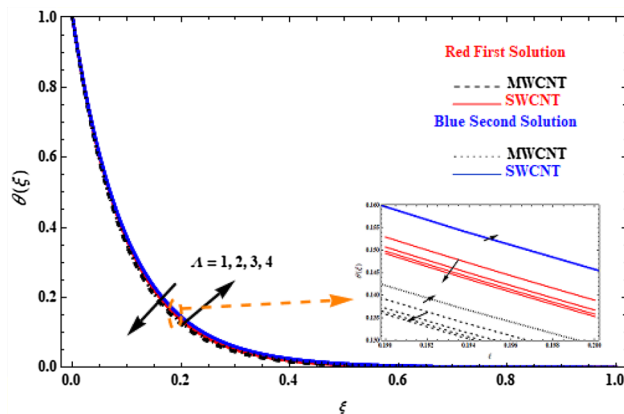


Figure 8. Plot of temperature $\theta(\xi)$ versus ξ for various values of Λ .

effect is observed in the lower branch solution (Fig. 7). This is because the higher values of Λ affects the dynamic viscosity, which results in a decrease in the yield stress and, thus, causes a resistance force that opposes to fluid mobility. The effect of Λ on temperature is small (Fig. 8). All upper branch solutions present smaller temperature with increasing Λ , while lower branch solutions present the reverse behaviour when Λ increases.

The investigation of the variation of nanoparticle volume fraction, ϕ , is presented in Figs. 9 and 10. In Fig. 9, as ϕ varies from 0.1 to 0.15 and 0.2, the velocity of the upper branch solution decreases, while velocity for the lower branch increases. We also observe higher SWCNT velocities on the upper branch and smaller on the lower branch, compared to MWCNT. It is of importance to note that ϕ has significant effect on temperature values,

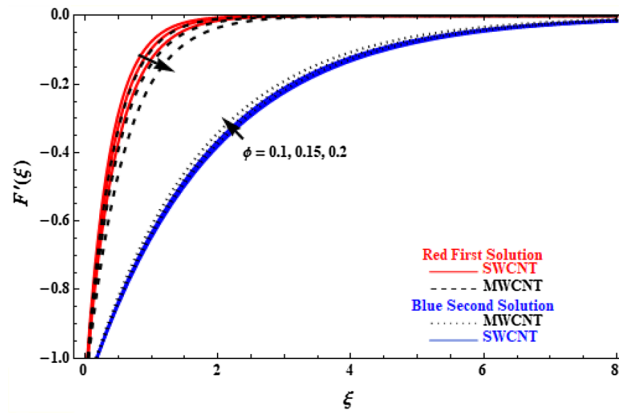


Figure 9. Plot of velocity $F'(\xi)$ versus ξ for various values of ϕ .

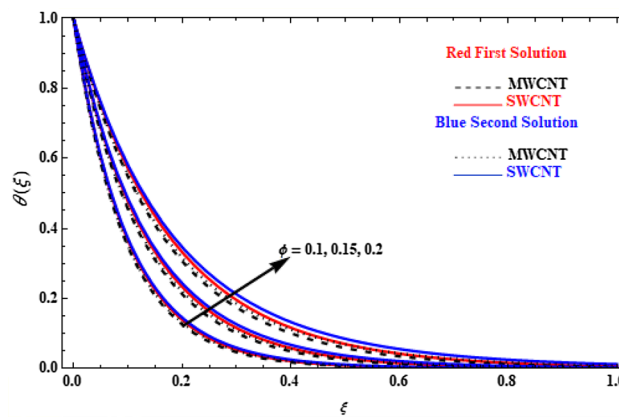


Figure 10. Plot of temperature $\theta(\xi)$ versus ξ for various values of ϕ .

since temperature of SWCNT and MWCNT of both upper and lower branch solutions increase with increasing ϕ . Moreover, SWCNT has given higher temperature values compared to MWCNT (Fig. 10). This is due to the addition of more nanoparticles which serve as heat transfer agents and causes temperature to rise with increasing value of ϕ .

The effect of the thermal radiation, N_r , on the temperature profiles for our model is depicted in Fig. 11. All profiles present higher values with increasing N_r , while, the SWCNT cases have slightly higher values than MWCNT. This is because the thermal radiation transfers more heat than any other parameter shown before. In

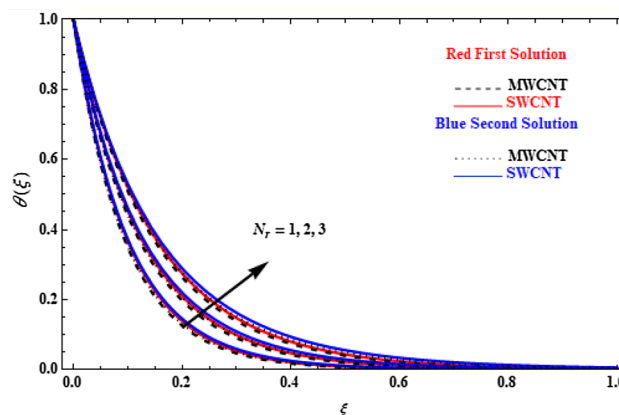


Figure 11. Plot of temperature $\theta(\xi)$ versus ξ for various values of N_r .

physical terms, the thermal conductivity of CNTs increases with the increase of the radiation parameter, and, as a result, the thermal boundary-layer thickness and the profiles of temperature increase.

In the presence of SWCNTs and MWCNTs, the skin friction coefficient versus M (Fig. 12) has shown that multiple solution exists only for the shrinking of the sheet. With increasing shrinking parameter values, the skin friction coefficient increases in both branches of the solution. In most cases, this occurs because the motion of the fluid is decreased when the shrinking parameter is increased. As a result, the velocity and skin friction obey to the inverse proportional relationship. Hence, this fact leads to the outcome that skin friction coefficient increases in presence of CNTs.

Figure 13 presents the dual solution for the skin friction coefficient versus V_c , for various values of M . The skin friction coefficient of SWCNTs and MWCNTs decreases as the suction parameter decreases and increases when the injection parameter increases, as a consequence of increasing the magnetic field M . It also has to be specified that the skin friction coefficient approaches zero value in case of high injection speed, while it increases exponentially at higher suction velocity. Furthermore, greater M values have an incremental effect on the shear stress. The behaviour of skin friction coefficient on SWCNTs and MWCNTs for various V_c values can be summarized by the fact that suction causes greater velocity gradients at the surface, whereas injection minimises them.

Figure 14 presents the dual solution for skin friction coefficient versus d for various M values. The skin friction coefficient of SWCNTs and MWCNTs increases as d decreases because the velocity gradients are larger when the plate decreases quicker or is stretched at a slower pace. Hence, at large values of the magnetic field, the skin friction coefficients of SWCNTs and MWCNTs increases, and this is due to the greater fluid velocity observed when the magnetic field value increases. Thus, the skin friction coefficients of SWCNTs and MWCNTs are proportionally increasing with the magnetic field.

Validation. The research has revealed that the SWCNTs achieve higher temperature than MWCNTs on non-Newtonian Casson fluid model on porous shrinking sheet. The dual solution obtained opens the pathway to future studies of Casson fluid flows under the impact of an inclined MHD, radiation and mass transpiration.

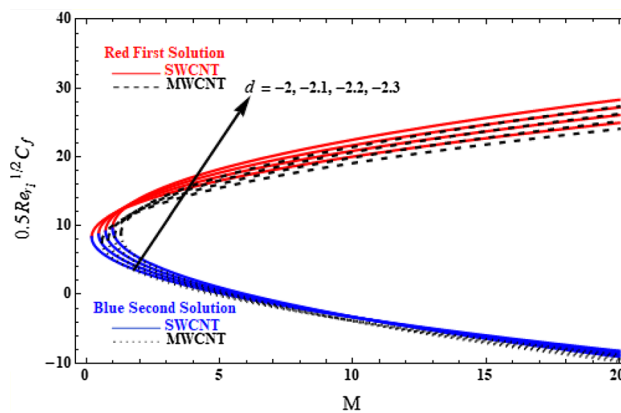


Figure 12. Plot of $0.5Re_1^{1/2} C_f$ versus M for various values of d .

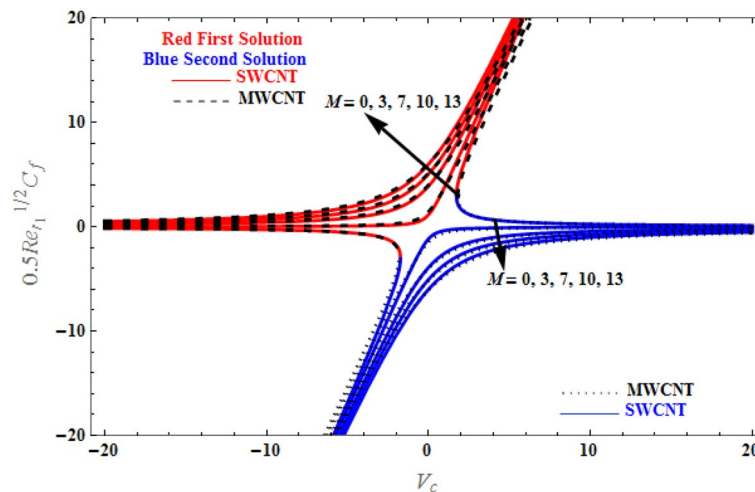


Figure 13. Plot of $0.5Re_1^{1/2} C_f$ versus V_c for various values of M .

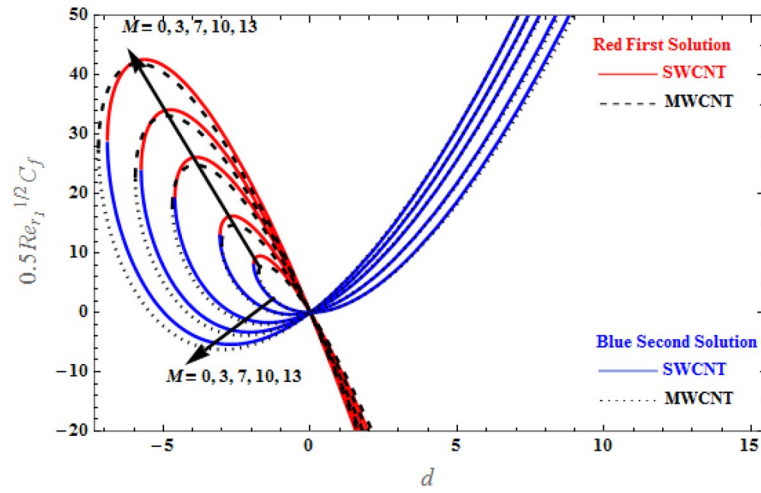


Figure 14. Plot of $0.5Re_{r1}^{1/2} C_f$ versus d for various values of M .

Authors	Fluid	Value of β
Crane ¹⁴	Newtonian	$\beta = 1$
Khan et al. ³⁴	Newtonian	$f(\eta) = f_w + \frac{\lambda}{\beta_\alpha} (1 - e^{-\beta_\alpha \xi}),$ $\frac{\mu_{hnf}}{\mu_f} \beta_\alpha^2 - 3 \frac{\rho_{hnf}}{\rho_f} \beta_\alpha f_w - \left(3 \frac{\rho_{hnf}}{\rho_f} \lambda + \frac{\sigma_{hnf}}{\sigma_f} M \right) = 0,$ and the roots are $\beta_\alpha = \frac{3 \frac{\rho_{hnf}}{\rho_f} f_w \pm \sqrt{9 f_w^2 \left(\frac{\rho_{hnf}}{\rho_f} \right)^2 + 4 \frac{\mu_{hnf}}{\mu_f} \left(3 \frac{\rho_{hnf}}{\rho_f} \lambda + \frac{\sigma_{hnf}}{\sigma_f} M \right)}}{2 \frac{\mu_{hnf}}{\mu_f}}$ Skin friction $0.5Re_{r1}^{1/2} C_f = \frac{\mu_{hnf}}{\mu_f} F''(0)$
Present work	Non-Newtonian (Casson fluid)	$F(\xi) = V_c + \frac{d}{\beta} (1 - Exp[-\beta \xi]).$ $A_1 \left(1 + \frac{1}{\lambda} \right) \beta^2 - 3A_2 V_c \beta - (A_5 M + 3A_2 d) = 0,$ and the roots are $\beta = \frac{3V_c A_2 \pm \sqrt{9V_c^2 A_2^2 - 4 \left(1 + \frac{1}{\lambda} \right) A_1 (-3dA_2 - MA_5)}}{2 \left(1 + \frac{1}{\lambda} \right) A_1}$ Skin friction $0.5Re_{r1}^{1/2} C_f = \frac{\mu_{nf} \left(1 + \frac{1}{\lambda} \right)}{\mu_f} F''(0)$

Table 2. Comparison to existing methods.

Approaches	Fluids	Stability analysis (Stable /unstable)
Hamid et al. ⁴⁷	Non-Newtonian	$\left(1 + \frac{1}{\lambda} \right) \frac{\partial^3 F}{\partial \eta^3} + F_0 \frac{\partial^2 F}{\partial \eta^2} + \left(\frac{\partial F}{\partial \eta} \right)^2 - M \frac{\partial F}{\partial \eta} - \frac{\partial^2 F}{\partial \tau \partial \mu \eta} = 0,$ $\frac{1}{Pr(1+R_d) \frac{\partial^2 \varphi}{\partial \eta^2} + \frac{\partial \varphi}{\partial \eta} \frac{\partial \varphi}{\partial \xi}}$
Khashi'ie et al. ⁴⁹	Newtonian	$\frac{\mu_{hnf}}{\mu_f} \frac{\partial^3 F}{\partial \eta^3} + 2f_0 \frac{\partial^2 F}{\partial \eta^2} + 2F_0 \frac{\partial^2 f_0}{\partial \eta^2} - \left(2f_0' - \gamma + \left(\frac{\sigma_{hnf}}{\sigma_f} \right) M \right) \frac{\partial F}{\partial \eta} = 0,$ $\frac{1}{Pr \frac{(\kappa)_{hnf}}{(\rho Cp)_{hnf}} \frac{(\kappa)_f}{(\rho Cp)_f} \frac{\partial^2 G}{\partial \eta^2} + \frac{\partial \theta_0}{\partial \eta} \frac{\partial G}{\partial \eta} + \frac{\partial G}{\partial \eta} \frac{\partial F}{\partial \eta}}$ $- \left(2 \frac{\partial f_0}{\partial \eta} - \gamma \right) G + 2 \left(\frac{\sigma_{hnf} / \sigma_f}{(\rho Cp)_{hnf} / (\rho Cp)_f} \right) EcM \frac{\partial f_0}{\partial \eta} \frac{\partial F}{\partial \eta} = 0,$
Present work	Non-Newtonian	$A_1 \left(1 + \frac{1}{\lambda} \right) \frac{\partial^3 f}{\partial \xi^3} + 3A_2 F_0 \frac{\partial^2 f}{\partial \xi^2} + 3A_2 F_0'' - A_2 (6F_0' - \gamma) \frac{\partial f}{\partial \xi} - A_5 M \frac{\partial f}{\partial \xi} - A_2 \frac{\partial^2 F}{\partial \xi \partial \epsilon} = 0,$ $(A_4 + N_r) \frac{\partial^2 \varphi}{\partial \xi^2} + 3A_3 Pr F_0 \frac{\partial \varphi}{\partial \xi} + 3A_3 Pr f_0' + \gamma \varphi - A_3 Pr \frac{\partial \varphi}{\partial \epsilon} = 0,$

Table 3. Comparison of the stability analysis with similar works.

M	First solution (upper branch solution)				Second solution (lower branch solution)			
	$d = -2$	$d = -2.1$	$d = -2.2$	$d = -2.3$	$d = -2$	$d = -2.1$	$d = -2.2$	$d = -2.3$
SWCNT								
0	8.35744	8.77532	9.19319	9.61106	8.35744	8.77532	9.19319	9.61106
5	16.5273	17.1174	17.6778	18.2069	0.187634	0.433234	0.708546	1.01525
10	20.0258	20.8629	21.682	22.4826	-3.31094	-3.31227	-3.29559	-3.26047
15	22.6947	23.6961	24.6835	25.6568	-5.97979	-6.14544	-6.29713	-6.43465
20	24.9394	26.0712	27.1913	28.2994	-8.22452	-8.52059	-8.80487	-9.07726
MWCNT								
0	7.63535	8.01712	8.39889	8.78065	7.63535	8.01712	8.39889	8.78065
5	15.4751	16.0240	16.5447	17.0355	-0.20443	0.010218	0.253092	0.525776
10	19.0751	19.8759	20.6600	21.4271	-3.80438	-3.84162	-3.86220	-3.86575
15	21.7871	22.7531	23.7062	24.6463	-6.51642	-6.71886	-6.90846	-7.08503
20	24.0572	25.1539	26.2397	27.3146	-8.78652	-9.11964	-9.44194	-9.75333

Table 4. Skin friction coefficient, $Re_1^{1/2} C_f$, for various values of d and M .

The velocity behaviour in the absence of Casson fluid and $M = 0$ in the presence of stretching plate results are converted¹⁴, while $\sin(\tau) = 1$ in the presence of hybrid nano particles leads to the results of Khan et al.³⁴.

Table 2 presents relevant works from the literature for comparison.

Table 3 presents the comparison of the stability analysis performed here with other works that have conducted the stability analysis with a time variable. Khashi'ie et al.⁴⁹ and Hamid et al.⁴⁷ have taken $\tau = ct$, while, in the present work, we have considered $\varepsilon = r_1^2 bt$.

Finally, in Table 4, values of skin friction coefficients both for the upper and lower branch solutions, related to Fig. 12, are presented.

Conclusion

This paper has presented a detailed investigation of the boundary-layer flow and heat transfer properties implied by water-based CNTs over a permeable shrinking sheet, affected by the parameters of the Casson fluid, an inclined magnetic field and thermal radiation effects. The exact solutions for velocity and temperature have been obtained with aid of the Gamma function. The analytical results have been graphically illustrated versus various dimensionless physical characteristics that have been found to affect velocity, shear stress, and temperature distribution.

- The velocity profile of the upper branch solution of SWCNT and MWCNT nanoparticles has obtained higher values when mass transpiration (V_c) and magnetic field (M) increase, but the opposite behaviour is observed for the lower branch solutions. Temperature values, on the other hand, have shown similar decreasing behaviour for both branches.
- The velocity profile also increases when Λ increases. The reverse behaviour appears for the lower branch solutions, while temperature is clearly decreased for upper branch solutions and increased for lower branch solutions.
- The fluid velocity of upper and lower branch solutions of all CNT nanoparticles decreases and increases, respectively. Furthermore, the temperature of both branch solutions obtains higher values when ϕ increases.
- The temperature for both branch solutions of CNT nanoparticles increases when the thermal radiation N_r increases. Moreover, it is observed that SWCNTs achieve higher temperatures compared to MWCNTs.
- The skin friction coefficient both carbon nanotubes increases for decreasing d and increases with M .

To conclude, we believe that the main findings of this analytical investigation can find field of applicability in various engineering and industrial applications, concerning medical applications, micro-fluidic devices, nanofluidic pumps, and space technology, among others.

Data availability

The datasets used and/or analysed during the current study available from the corresponding author on reasonable request.

Received: 6 January 2023; Accepted: 23 February 2023

Published online: 27 February 2023

References

1. Guedri, K. et al. Insight into the heat transfer of third-grade micropolar fluid over an exponentially stretched surface. *Sci. Rep.* **12**, 15577 (2022).
2. Lin, Y., Jia, Y., Alva, G. & Fang, G. Review on thermal conductivity enhancement, thermal properties and applications of phase change materials in thermal energy storage. *Renew. Sustain. Energy Rev.* **82**, 2730–2742 (2018).
3. Kumanek, B. & Janas, D. Thermal conductivity of carbon nanotube networks: a review. *J. Mater. Sci.* **54**, 7397–7427 (2019).

4. Iijima, S. Helical microtubules of graphitic carbon. *Nature* **354**, 56–58 (1991).
5. Mahabaleshwar, U. S., Sneha, K. N. & Huang, H.-N. An effect of MHD and radiation on CNTs-Water based nanofluids due to a stretching sheet in a Newtonian fluid. *Case Stud Thermal Eng* **28**, 101462 (2021).
6. Sneha, K. N., Mahabaleshwar, U. S., Chan, A. & Hatami, M. Investigation of radiation and MHD on non-Newtonian fluid flow over a stretching/shrinking sheet with CNTs and mass transpiration. *Waves Random Complex Med.* <https://doi.org/10.1080/17455030.2022.2029616> (2022).
7. Hussain, Z., Hayat, T., Alsaedi, A. & Anwar, M. S. Mixed convective flow of CNTs nanofluid subject to varying viscosity and reactions. *Sci. Rep.* **11**, 22838 (2021).
8. Mahabaleshwar, U. S., Sneha, K. N., Chan, A. & Zeidan, D. An effect of MHD fluid flow heat transfer using CNTs with thermal radiation and heat source/sink across a stretching/shrinking sheet. *Int. Commun. Heat Mass Transfer* **135**, 106080 (2022).
9. Rasool, G., Wakif, A., Wang, X., Shafiq, A. & Chamkha, A. J. Numerical passive control of alumina nanoparticles in purely aquatic medium featuring EMHD driven non-Darcian nanofluid flow over convective Riga surface. *Alex. Eng. J.* <https://doi.org/10.1016/j.aej.2022.12.032> (2022).
10. Rasool, G. *et al.* Darcy-forchheimer flow of water conveying multi-walled carbon nanoparticles through a vertical Cleveland Z-staggered cavity subject to entropy generation. *Micromachines* **13**, 744 (2022).
11. Batool, S. *et al.* Numerical analysis of heat and mass transfer in micropolar nanofluids flow through lid driven cavity: finite volume approach. *Case Stud. Thermal Eng.* **37**, 102233 (2022).
12. Sakiadis, B. C. Boundary-layer behavior on continuous solid surfaces: I. Boundary-layer equations for two-dimensional and axisymmetric flow. *AIChE J.* **7**, 26–28 (1961).
13. Sakiadis, B. C. Boundary-layer behavior on continuous solid surfaces: II. The boundary layer on a continuous flat surface. *AIChE J.* **7**, 221–225 (1961).
14. Crane, L. J. Flow past a stretching plate. *J. Appl. Math. Phys. (ZAMP)* **21**, 645–647 (1970).
15. Saeed, A. *et al.* Influence of Cattaneo-Christov heat flux on MHD Jeffrey, Maxwell, and Oldroyd-B nanofluids with homogeneous-heterogeneous reaction. *Symmetry* **11**, 439 (2019).
16. Reddy, C. S., Naikoti, K. & Rashidi, M. M. MHD flow and heat transfer characteristics of Williamson nanofluid over a stretching sheet with variable thickness and variable thermal conductivity. *Trans. A Razmadze Math. Inst.* **171**, 195–211 (2017).
17. Akhtar, S. *et al.* Analytical solutions of PDEs by unique polynomials for peristaltic flow of heated Rabinowitsch fluid through an elliptic duct. *Sci. Rep.* **12**, 12943 (2022).
18. Casson, N. A flow equation for pigment-oil suspensions of the printing ink type. in (1959).
19. Ibrar, N., Reddy, M. G., Shehzad, S. A., Sreenivasulu, P. & Poornima, T. Interaction of single and multi walls carbon nanotubes in magnetized-nano Casson fluid over radiated horizontal needle. *SN Appl. Sci.* **2**, 677 (2020).
20. Mahabaleshwar, U. S., Aly, E. H. & Vishalakshi, A. B. MHD and thermal radiation flow of graphene Casson nanofluid stretching/shrinking sheet. *Int. J. Appl. Comput. Math* **8**, 113 (2022).
21. Vaidya, H., Rajashekhar, C., Manjunatha, G. & Prasad, K. V. Effects of heat transfer on peristaltic transport of a bingham fluid through an inclined tube with different wave forms. *Defect Diffus. Forum* **392**, 158–177 (2019).
22. Bhattacharyya, K., Uddin, M. S. & Layek, G. C. Exact solution for thermal boundary layer in Casson fluid flow over permeable shrinking sheet with variable wall temperature and thermal radiation. *Alex. Eng. J.* **55**, 1703–1712 (2016).
23. Li, X. *et al.* Thermal performance of iron oxide and copper (Fe₃O₄, Cu) in hybrid nanofluid flow of Casson material with Hall current via complex wavy channel. *Mater. Sci. Eng. B* **289**, 116250 (2023).
24. Megahed, A. M., Reddy, M. G. & Abbas, W. Modeling of MHD fluid flow over an unsteady stretching sheet with thermal radiation, variable fluid properties and heat flux. *Math. Comput. Simul.* **185**, 583–593 (2021).
25. Reddy, P. C., Umamheshwar, M., Reddy, S. H., Raju, A. B. M. & Raju, M. C. Numerical study on the parabolic flow of MHD fluid past a vertical plate in a porous medium. *Heat Transf.* **51**, 3418–3430 (2022).
26. Alam, J., Murtaza, M. G., Tzirtzilakis, E. E. & Ferdows, M. Application of biomagnetic fluid dynamics modeling for simulation of flow with magnetic particles and variable fluid properties over a stretching cylinder. *Math. Comput. Simul.* **199**, 438–462 (2022).
27. Sarada, K., Gowda, R. J. P., Sarris, I. E., Kumar, R. N. & Prasannakumara, B. C. Effect of magnetohydrodynamics on heat transfer behaviour of a non-newtonian fluid flow over a stretching sheet under local thermal non-equilibrium condition. *Fluids* **6**, 264 (2021).
28. Devi, S. S. U. & Devi, S. P. A. Numerical investigation of three-dimensional hybrid Cu–Al₂O₃/water nanofluid flow over a stretching sheet with effecting Lorentz force subject to Newtonian heating. *Can. J. Phys.* **94**, 490–496 (2016).
29. Shafiq, A., Zari, I., Rasool, G., Tlili, I. & Khan, T. S. On the MHD Casson axisymmetric marangoni forced convective flow of nanofluids. *Mathematics* **7**, 1087 (2019).
30. Bhattacharyya, K. & Layek, G. C. Effects of suction/blowing on steady boundary layer stagnation-point flow and heat transfer towards a shrinking sheet with thermal radiation. *Int. J. Heat Mass Transf.* **54**, 302–307 (2011).
31. Bhattacharyya, K., Mukhopadhyay, S., Layek, G. C. & Pop, I. Effects of thermal radiation on micropolar fluid flow and heat transfer over a porous shrinking sheet. *Int. J. Heat Mass Transf.* **55**, 2945–2952 (2012).
32. Turkyilmazoglu, M. A note on micropolar fluid flow and heat transfer over a porous shrinking sheet. *Int. J. Heat Mass Transf.* **72**, 388–391 (2014).
33. Aly, E. H. Dual exact solutions of graphene–water nanofluid flow over stretching/shrinking sheet with suction/injection and heat source/sink: critical values and regions with stability. *Powder Technol.* **342**, 528–544 (2019).
34. Khan, U. *et al.* Exact solutions for MHD axisymmetric hybrid nanofluid flow and heat transfer over a permeable non-linear radially shrinking/stretching surface with mutual impacts of thermal radiation. *Eur. Phys. J. Special Top.* **231**(6), 1195–1204. <https://doi.org/10.1140/epjs/s11734-022-00529-2> (2022).
35. Ullah, I. *et al.* MHD slip flow of Casson fluid along a nonlinear permeable stretching cylinder saturated in a porous medium with chemical reaction, viscous dissipation, and heat generation/absorption. *Symmetry* **11**, 531 (2019).
36. Ali, A., Marwat, D. N. K. & Asghar, S. Viscous flow over a stretching (shrinking) and porous cylinder of non-uniform radius. *Adv. Mech. Eng.* **11**, 1687814019879842 (2019).
37. Reboucas, R. B. & Loewenberg, M. Near-contact approach of two permeable spheres. *J. Fluid Mech.* <https://doi.org/10.1017/jfm.2021.588> (2021).
38. Mandal, S. & Shit, G. C. Entropy analysis on unsteady MHD biviscosity nanofluid flow with convective heat transfer in a permeable stretchable rotating disk. *Chin. J. Phys.* **74**, 239–255 (2021).
39. Rashed, A. S., Mahmoud, T. A. & Wazwaz, A.-M. Axisymmetric forced flow of nonhomogeneous nanofluid over heated permeable cylinders. *Waves Random Complex Media* <https://doi.org/10.1080/17455030.2022.2053611> (2022).
40. Li, W., Jia, X., Feng, F. & Xu, Z. Axisymmetric transient response of a cylindrical cavity in an unsaturated poroelastic medium. *J. Sound Vib.* **524**, 116763 (2022).
41. Khan, U. *et al.* Agrawal axisymmetric rotational stagnation-point flow of a water-based molybdenum disulfide-graphene oxide hybrid nanofluid and heat transfer impinging on a radially permeable moving rotating disk. *Nanomaterials* **12**, 787 (2022).
42. Turkyilmazoglu, M. Existence of exact algebraic solutions for viscous flow and heat transfer. *J. Thermophys. Heat Transf.* **28**, 150–154 (2014).
43. Turkyilmazoglu, M. Radially expanding/contracting and rotating sphere with suction. *Int. J. Numer. Meth. Heat Fluid Flow* **32**, 3439–3451 (2022).

44. Wahid, N. S., Arifin, N. M., Turkyilmazoglu, M., Hafidzuddin, M. E. H. & Abd Rahmin, N. A. MHD hybrid Cu–Al₂O₃/water nanofluid flow with thermal radiation and partial slip past a permeable stretching surface: analytical solution. *J. Nano Res* **64**, 75–91 (2020).
45. Merkin, J. H. On dual solutions occurring in mixed convection in a porous medium. *J. Eng. Math.* **20**, 171–179 (1986).
46. Harris, S. D., Ingham, D. B. & Pop, I. Mixed convection boundary-layer flow near the stagnation point on a vertical surface in a porous medium: Brinkman model with slip. *Transp. Porous Med* **77**, 267–285 (2009).
47. Hamid, M., Usman, M., Khan, Z. H., Ahmad, R. & Wang, W. Dual solutions and stability analysis of flow and heat transfer of Casson fluid over a stretching sheet. *Phys. Lett. A* **383**, 2400–2408 (2019).
48. Roşca, N. C., Roşca, A. V. & Pop, I. Axisymmetric flow of hybrid nanofluid due to a permeable non-linearly stretching/shrinking sheet with radiation effect. *Int. J. Numer. Meth. Heat Fluid Flow* **31**, 2330–2346 (2020).
49. Khashiie, N. S. *et al.* Magnetohydrodynamics (MHD) axisymmetric flow and heat transfer of a hybrid nanofluid past a radially permeable stretching/shrinking sheet with Joule heating. *Chin. J. Phys.* **64**, 251–263 (2020).

Author contributions

Conceptualization: U.S.M.; methodology: U.S.M. and F.S.; software: R.M. and U.S.M.; formal analysis: F.S., R.M. and U.S.M.; investigation: R.M., U.S.M. and F.S.; writing—original draft preparation: U.S.M.; writing—review and editing: F.S. All authors have read and agreed to the published version of the manuscript.

Competing interests

The authors declare no competing interests.

Additional information

Correspondence and requests for materials should be addressed to F.S.

Reprints and permissions information is available at www.nature.com/reprints.

Publisher's note Springer Nature remains neutral with regard to jurisdictional claims in published maps and institutional affiliations.



Open Access This article is licensed under a Creative Commons Attribution 4.0 International License, which permits use, sharing, adaptation, distribution and reproduction in any medium or format, as long as you give appropriate credit to the original author(s) and the source, provide a link to the Creative Commons licence, and indicate if changes were made. The images or other third party material in this article are included in the article's Creative Commons licence, unless indicated otherwise in a credit line to the material. If material is not included in the article's Creative Commons licence and your intended use is not permitted by statutory regulation or exceeds the permitted use, you will need to obtain permission directly from the copyright holder. To view a copy of this licence, visit <http://creativecommons.org/licenses/by/4.0/>.

© The Author(s) 2023